Supporting Information

Mg^{2+} Initiated in-situ Polymerization of Dioxolane Enabling Stable Interfaces in Solid-State Lithium Metal Batteries

Hao Xu[a,b,c], Jinshuo Mi[a,b,c]*, Jiabin Ma[a,b,c], Zhuo Han[a,b], Shun Lv[a,b], Likun Chen[a,b], Jiameng Zhang[a,b], Ke Yang[a,b], Boyu Li[a,b], Yuhang Li[a,b], Xufei An[a,b], Yuetao Ma[a,b], Shaoke Guo[a,b], Hai Su[a,b], Peiran Shi[a]*, Ming Liu[a], Feiyu Kang[a], Yan-Bing He[a]*

[a] Shenzhen All-Solid-State Lithium Battery Electrolyte Engineering Research Center, Institute of Materials Research (IMR), Tsinghua Shenzhen International Graduate School, Tsinghua University, Shenzhen 518055, China.

[b] School of Materials Science and Engineering, Tsinghua University, Beijing 100084, China.

[c] Contributed equally to this work.

*Corresponding authors. Email: mjs19@mails.tsinghua.edu.cn, shipeiran@sz.tsinghua.edu.cn, he.yanbing@sz.tsinghua.edu.cn

Table of Contents

Methods

Preparation of electrolytes

Electrolyte preparation and cell assembly were carried out in an argon-filled glove box with H_2O and O_2 levels maintained below 0.1 ppm. Three types of samples were prepared: liquid electrolytes (LE), $LiPF_6$-catalyzed PDOL polymer electrolytes (PDE), and MMT-catalyzed PDOL composite solid-state electrolytes (MPDE). The LE consisted of 1.8M LiTFSI (Guangdong Canrd New Energy Technology Co., Ltd., 99.9%) and 0.2M LiDFOB (DoDoChem, 99.9%) dissolved in DOL (Sigma-Aldrich, 99.9%). For PDE, 3 wt.% of $LiPF_6$ was added to LE to catalyze the polymerization of DOL. In the case of MPDE, 3 wt.% of montmorillonite (Aladin, 99%) was incorporated into the LE. The well-stirred precursor solution was completely polymerized in the stirrer bottle after 48 hours for PDE and 24 hours for MPDE at room temperature.

Cathode preparation and battery assembly

The preparation of the $LiNi_{0.8}Co_{0.1}Mn_{0.1}O_2$ (NCM811) cathode followed these steps. First, NCM811, Super P, and PVDF5130 were dried in an oven at 60 °C for 24 hours to remove residual moisture. Then, NCM811, Super P, and PVDF were combined in a mass ratio of 8:1:1 and mixed with N-Methylpyrrolidone (NMP). This mixture was stirred thoroughly for 4 hours until a homogeneous slurry was obtained. The slurry was evenly coated onto aluminum foil using a scraper of appropriate thickness and dried under vacuum at 120 °C for 2 hours. The dried cathodes were then punched into 12 mm diameter discs and stored under vacuum. The NCM811 loading for each cathode was approximately 1.0 mg cm^{-2}. For battery assembly, 40 μL of the well-stirred precursor solution was carefully dispensed into the battery to ensure complete wetting of the separator (Celgard 2500) and electrodes. The electrolyte was fully polymerized in the assembled cell after 48 hours at room temperature.

Electrochemical characterization

Electrochemical impedance spectroscopy (EIS) was applied to test ionic conductivities by an electrochemical station (Bio Logic Science Instruments, France) in a frequency

range of 7 MHz to 0.1 Hz. Ionic conductivities (σ) were derived from the following Equation:

$$\sigma = \frac{L}{RS}$$

The parameters are defined as follows: L is the thickness of the electrolytes, R is the bulk resistance of Li-ion migration, and S is the contact area of the stainless steel. The lithium-ion transfer numbers of PDE and MPDE were determined using the following equation. Specifically, I_s and I_0 correspond to the steady-state current and the initial current, respectively, in which Li/Li batteries were polarized by a voltage of ΔV = 20 mV for 10000 seconds. R_0 and R_s denote the interfacial resistance before and after polarization, respectively.

$$t_{Li+} = \frac{I_s(\Delta V - I_0 R_0)}{I_0(\Delta V - I_s R_s)}$$

Linear sweep voltammetry (LSV) of electrolytes was conducted on Li/stainless steel cells using impedance spectroscopy, with a scanning rate of 0.1 mV s^{-1} up to 6 V. The electrochemical properties of all samples were evaluated using the LAND CT2001A and NEWARE Battery Test System (CT-4008Tn-5V50Ma-164).

Characterizations

The ^{1}H NMR and ^{13}C NMR spectra of electrolytes were recorded using a Bruker 400 MHz AVANCE III spectrometer with dimethyl sulfoxide -d6 as the deuterated solvent. The functional groups of electrolytes were characterized by a Fourier transform infrared (FTIR) spectra spectrometer (VERTEX 70) and a Micro-laser confocal Raman spectrometer (Horiba LabRAM HR800, France). Scanning electron microscope (SEM; HITACH S4800) and Transmission electron microscope (TEM; FEI Tecnai F30) were used to analyze the morphologies of lithium deposition and the cathode electrolyte interphase (CEI). The composition of the solid electrolyte interphase (SEI) and CEI was determined using X-ray photoelectron spectroscopy (XPS; Ulvac-Phi PHI S000 Versa Probe II). The analysis of the CEI component and 3D distribution was performed using

time-of-flight secondary ion mass spectrometry (TOF-SIMS, PHI nanoTOF II, 30 keV, 2 nA) over a region of 200 μm×200 μm×50 nm, following 10 cycles of Li/NCM811 cells at 0.1 C and 25 °C. The roughness and Young's modulus of the SEI and CEI were measured using atomic force microscopy (AFM; Bruker Dimension Icon).

Density functional theory (DFT) calculations

HOMO and LUMO: The HOMO and LUMO was calculated by the the first-principles calculation, which was conducted in Gaussian 16 program with Becke's three-parameter hybrid method using the Lee-Yang-Parr correlation functional (B3LYP) at 6-311G* level and the dispersion was corrected by Grimme's DFT-D3 (BJ) program. The structures were obtained using the GaussView6.0 software.

Migration barrier: The density functional theory (DFT) calculations were conducted using the Vienna Ab Initio Package (VASP) with the Perdew-Burke-Ernzerhof (PBE) functional, which is a generalized gradient approximation. To describe the ionic cores, projected augmented wave (PAW) potentials were utilized, specifically potentials.[1-6] Valence electrons were represented using a set of plane-wave basis with a cutoff kinetic energy of 500 eV. The convergence of electronic energy was achieved when the total energy change decreased to less than 10^{-4} eV. For geometry optimization, a residual force threshold of 10^{-2} eV $Å^{-1}$ was set to ensure convergence. We modeled the surface using a symmetric periodic slab and a 15 Å vacuum layer was inserted between the slab and its periodic image. The atoms of the matrix slab are fixed to reduce the calculation only when the adsorption energy. The migration barriers were calculated using the Climbing Image Nudged Elastic Band (CI-NEB) method.[7] Convergence of the electronic energy was achieved when the total change in energy was less than 10^{-7} eV.

Binding Energy: The density functional theory (DFT) calculations were performed using the Vienna Ab Initio Package (VASP) with the generalized gradient approximation Perdew-Burke-Ernzerhof (GGA-PBE) functional. Projected augmented wave (PAW) potentials[1-6] were chosen to describe the ionic cores, and valence electrons

were described using plane wave basis set with a kinetic energy cutoff of 450 eV. We model the surface using a symmetric periodic slab, and a 15 Å vacuum layer was inserted between the slab and its periodic image. Partial occupancies of the Kohn-Sham orbitals were allowed using the Gaussian smearing method and a width of 0.05 eV. The electronic energy was considered self-consistent when the energy change was smaller than 10^{-5} eV. A geometry optimization was considered convergent when the force change was smaller than 0.05 eV/Å. Grimme's DFT-D3 methodology[8] was used to describe the dispersion interactions. The montmorillonite model, along with the specific substitution principles and the detailed modeling process, was established with hydrogen atoms added to compensate for the unsaturated bonds[9]. The energy error caused by the image charge is addressed under the boundary condition where counterions are used to eliminate periodicity.

The binding energy is computed as:

$$E_b = E_{total} - E_{sub} - E_{TFSI^-\ and\ Li^+}$$

where E_{sub} are the energy of the bare surfaces, respectively, and E_{total} was the total energy of the configurations.

Supporting Figures

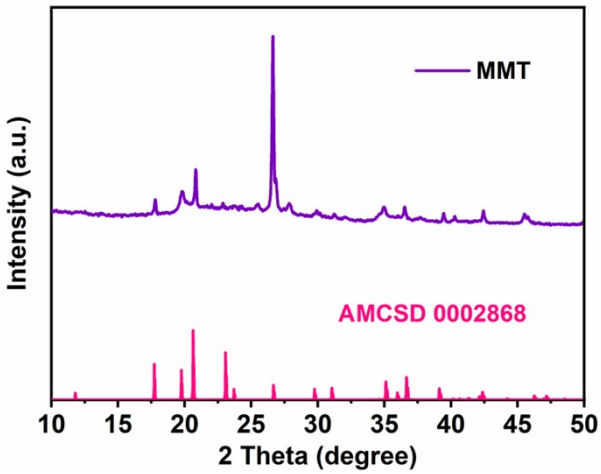

Fig. S1 The XRD analysis of montmorillonite filler.

Due to the disorder in montmorillonite structure, we utilize the Crystallographic Information File (CIF) data of montmorillonite from American Mineralogist Crystal Structure Database[10]. The result shows that the montmorillonite samples used in our work match well with AMCSD 0002868, indicating the structure integrity of montmorillonite filler.

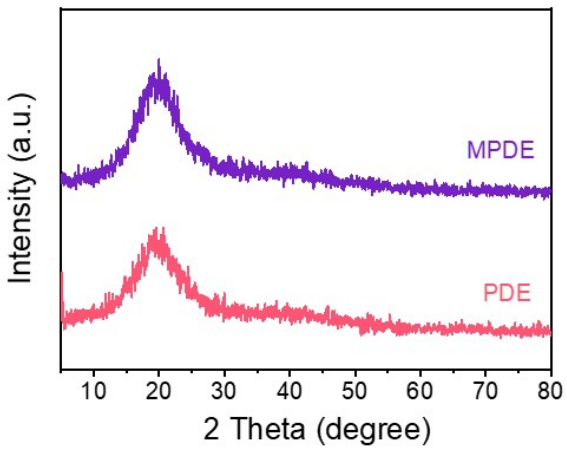

Fig. S2 The XRD analysis of PDE and MPDE.

The XRD patterns of MPDE remains unchanged after in-situ polymerization initiated by a Mg^{2+}-containing montmorillonite filler, comparing with that of PDE.

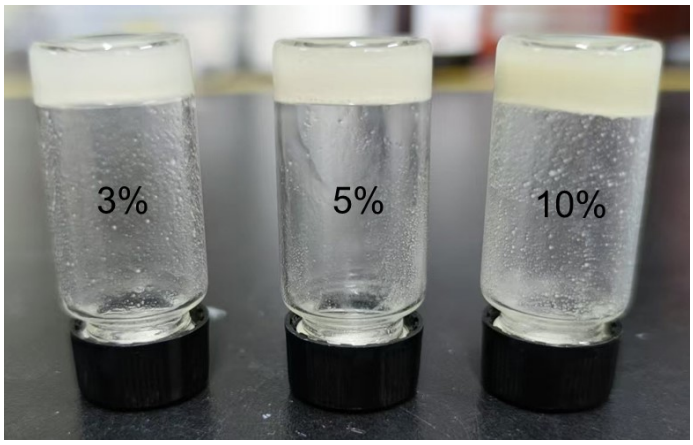

Fig. S3 Digital photograph depicting the solid-state PDOL electrolyte formed spontaneously in an electrolyte with 3 wt.%, 5 wt.%, and 10 wt.% MMT content.

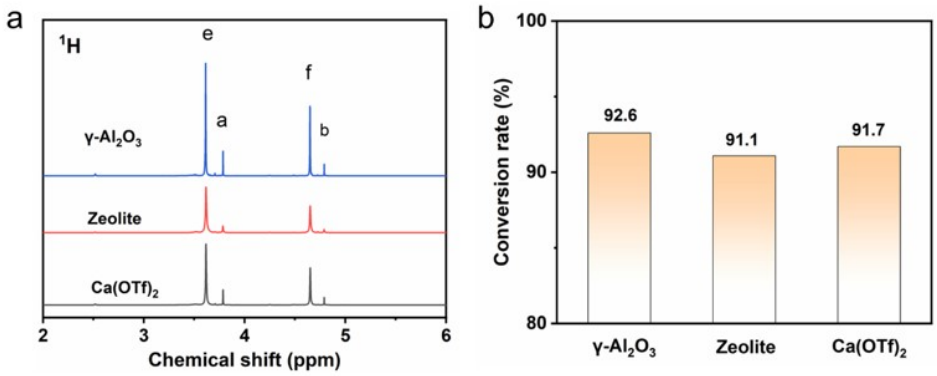

Fig. S4 (a) Hydrogen NMR spectra of γ-Al_2O_3, zeolite and $Ca(OTf)_2$ and (b) the corresponding conversion rate of DOL to PDOL.

We designed some experiments to study the conversion rates of DOL to PDOL by utilizing γ-Al_2O_3, zeolite and $Ca(OTf)_2$ inorganic fillers having Lewis acid sites as initiators. Nuclear magnetic resonance (NMR) analysis (Fig. S4a) confirms that these inorganic fillers all can initiate the ring-opening polymerization of DOL. After polymerization, the conversion rates can be estimated by integrating the peak area of the ^{1}H NMR spectra. The results show that the conversion rate of DOL using γ-Al_2O_3, zeolite and $Ca(OTf)_2$ is 92.6 %, 91.1% and 91.7 %, respectively (Fig. S4b).

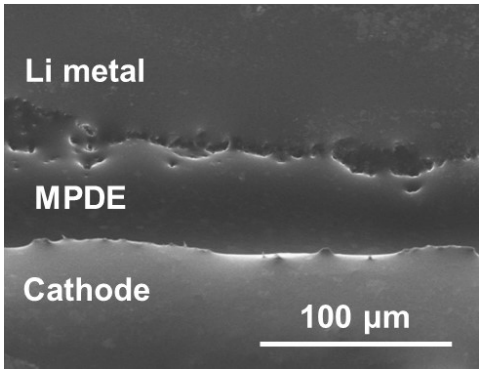

Fig. S5 The cross-sectional SEM image of NCM811/MPDE/Li battery.

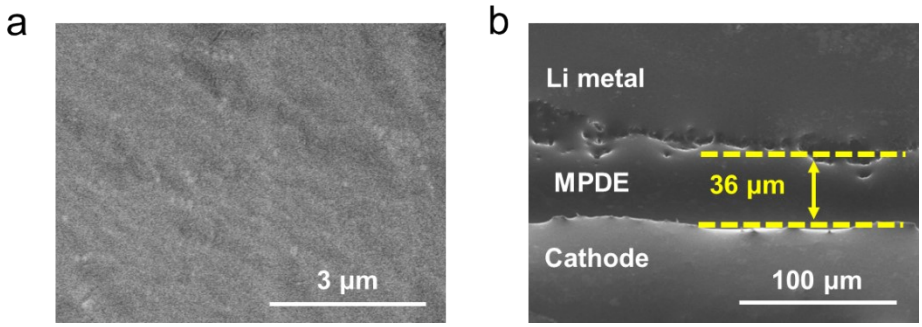

Fig. S6 (a) The morphology of MPDE surface and (b) the cross-sectional SEM image of NCM811/MPDE/Li battery.

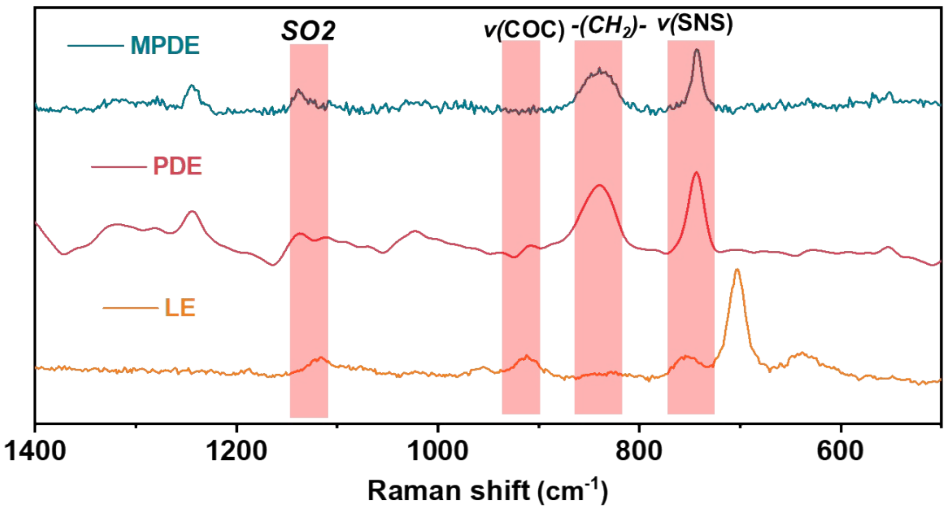

Fig. S7 Raman spectroscopy analysis of LE, PDE and MPDE.

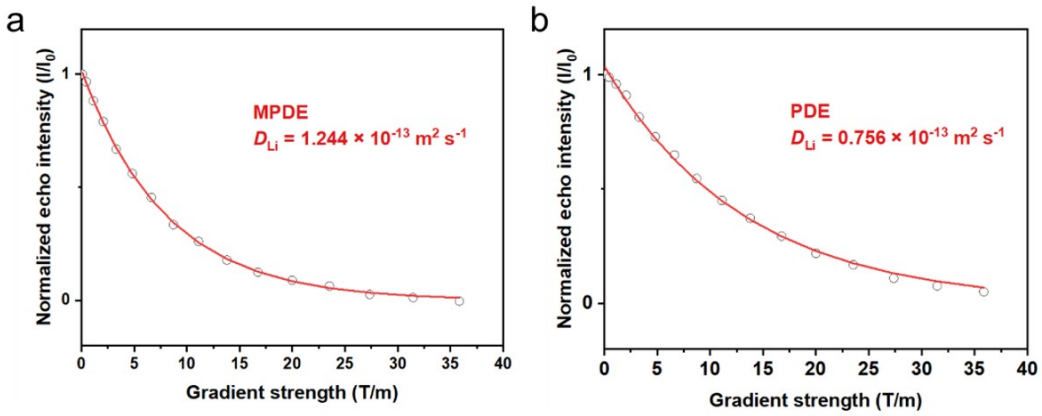

Fig. S8 PFG-NMR analysis of Li^+ self-diffusion coefficient in (a) MPDE and (b) PDE.

We performed the pulsed field gradient nuclear magnetic resonance (PFG-NMR) and fitted Li^+ self-diffusion coefficient (D_{Li}) with the TopSpin software. As shown in Fig. S8, the D_{Li} of MPDE is 1.244×10^{-13} m^2s^{-1}, higher than that of PDE (0.756×10^{-13} m^2s^{-1}), indicating the faster Li^+ diffusion in MPDE with uniform polymer chain length.

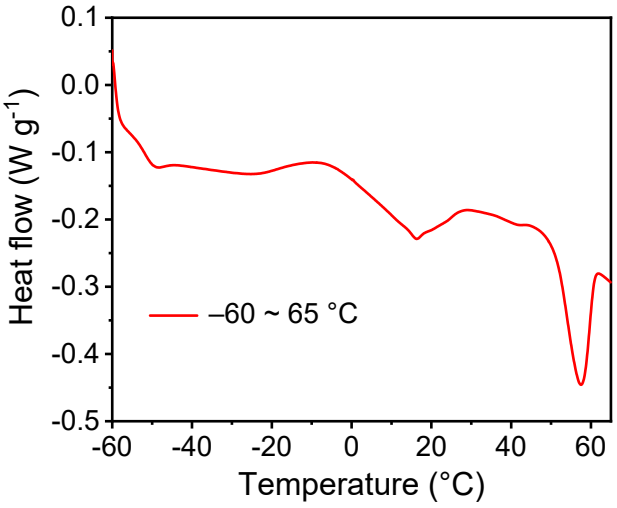

Fig. S9 Differential scanning calorimetry (DSC) analysis of MPDE.

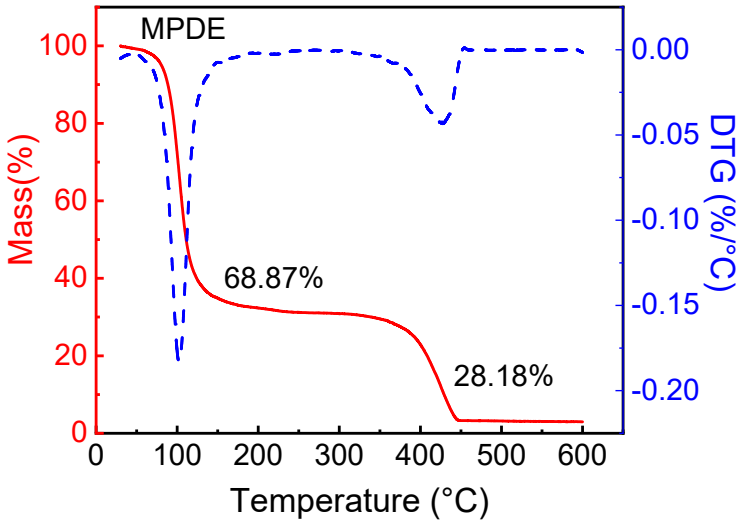

Fig. S10 Thermogravimetric analysis (TGA) analysis of MPDE.

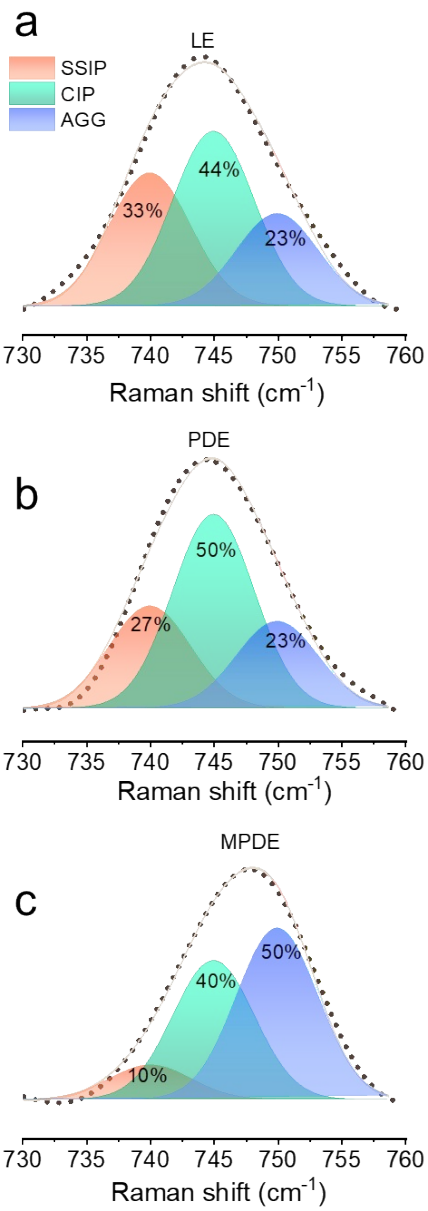

Fig. S11 Raman spectra of LE, PDE and MPDE, and the calculated proportions of anion aggregates (AGG, 752.5 cm^{-1}), contact ion pairs (CIP, 745.6 cm^{-1}), and solvent-separated ion pairs (SSIP, 740.9 cm^{-1}),which were analyzed by peak-fitting.

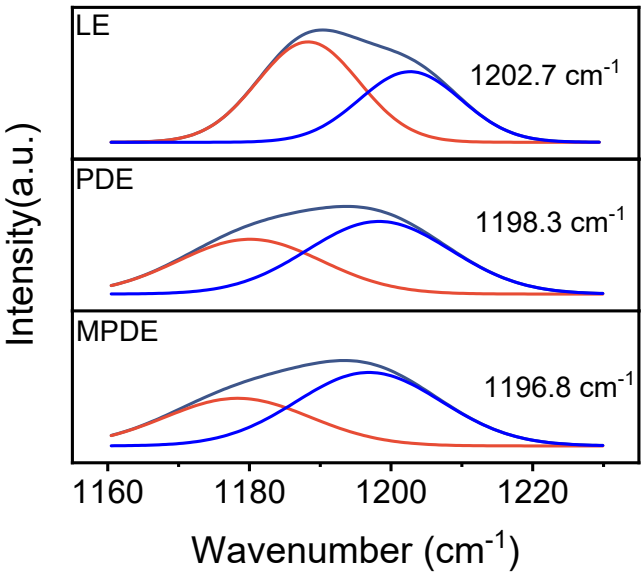

Fig. S12 FTIR spectroscopy analysis of CF_3 stretching vibration peak of LE, PDE and MPDE.

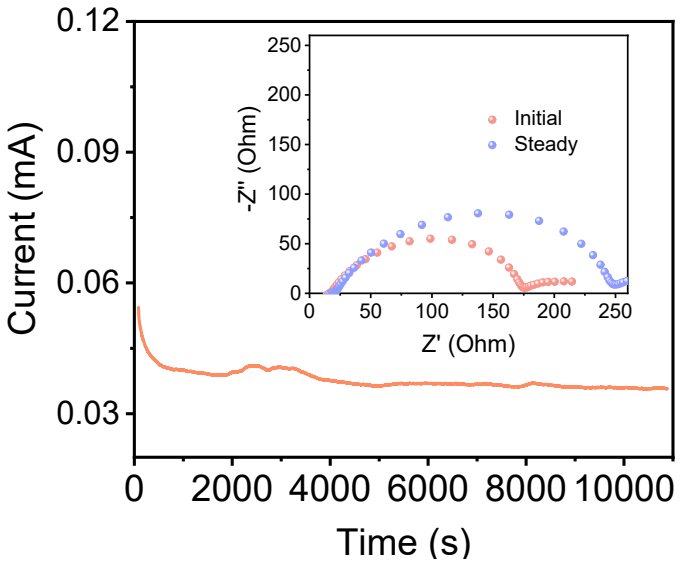

Fig. S13 The steady-state polarization curve of the lithium symmetric battery assembled by PDE, insets: the EIS curve before and after polarization.

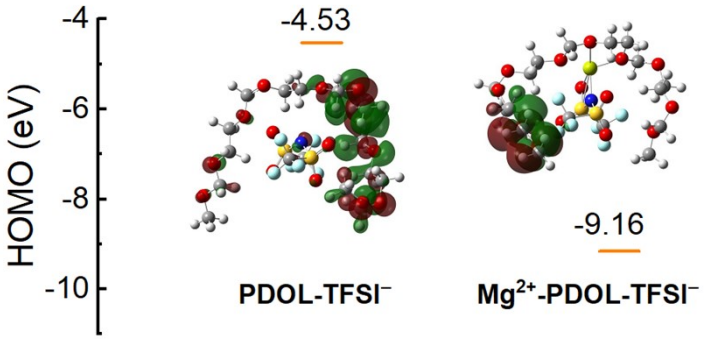

Fig. S14 Calculated HOMO energies and the corresponding optimized geometrical structures of PDOL-TFSI$^-$ and Mg^{2+}-PDOL-TFSI$^-$.

Density functional theory (DFT) calculations are also performed to assess the mechanism of Mg^{2+} increasing the oxidation stability by modulating interaction with TFSI. Compared to PDOL-TFSI$^-$ complex (-4.53 eV), the Mg^{2+}-PDOL-TFSI$^-$ complex shows a relatively lower HOMO energy of -9.16 eV, indicating its stronger antioxidative capacity.

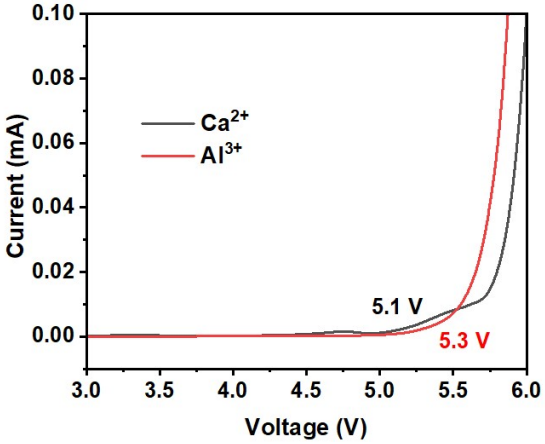

Fig. S15 LSV curves of Ca^{2+}-PDOL-TFSI complex and Al^{3+}-PDOL-TFSI complex.

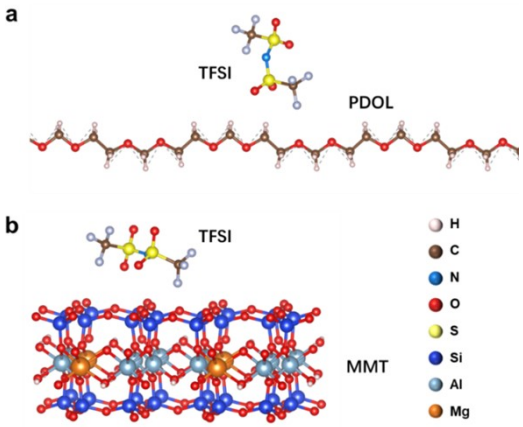

Fig. S16 The binding energy of TFSI anion with (a) PDOL and (b) MMT by DFT calculations.

The calculation results show that the binding energy of TFSI anion with PDOL is -0.67 eV, the value of TFSI anion with MMT is -2.06 eV, indicating MMT has stronger binding force with TFSI anions compared with PDOL, thus also contributes to the oxidation stability of PDOL-TFSI complex.

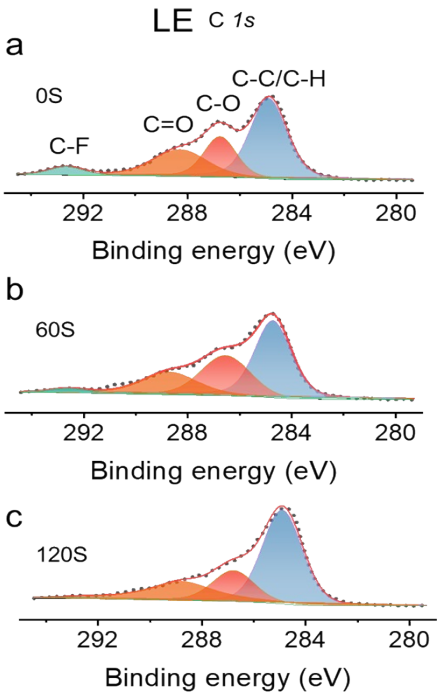

Fig. S17 The C *1s* XPS results for NCM811 cathode cycling with LE at different etching times.

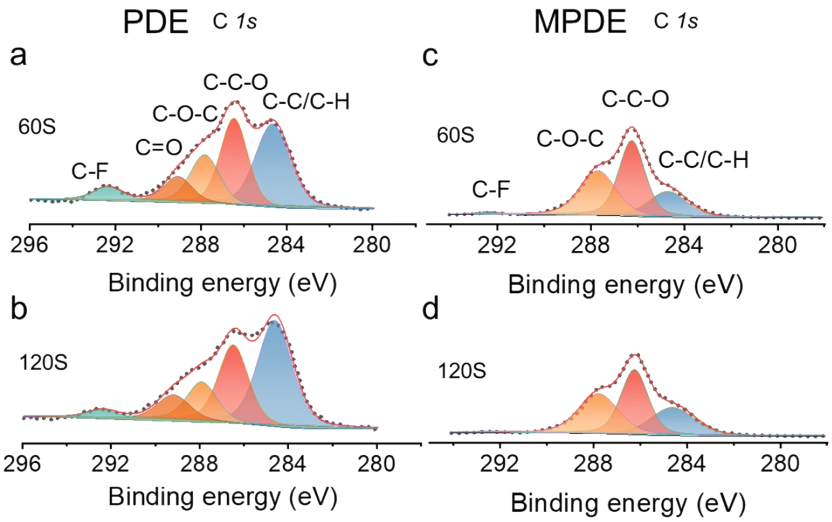

Fig. S18 The C *1s* XPS results for NCM811 cathodes cycling with PDE and MPDE at different etching times.

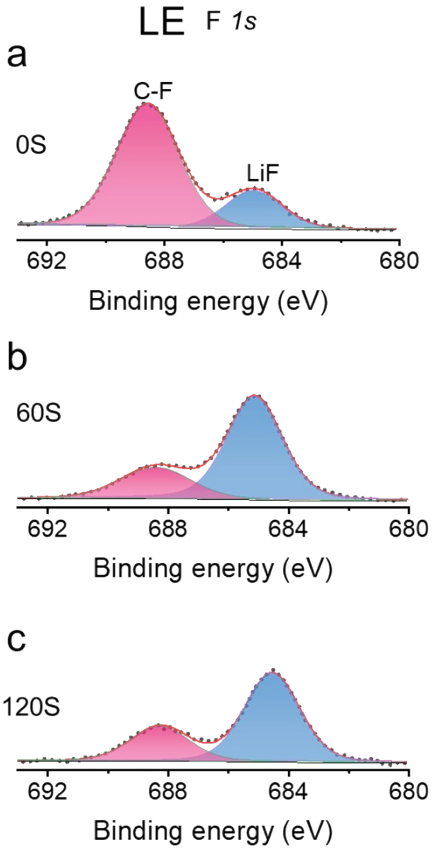

Fig. S19 The F *1s* XPS results for NCM811 cathodes cycling with LE at different etching times.

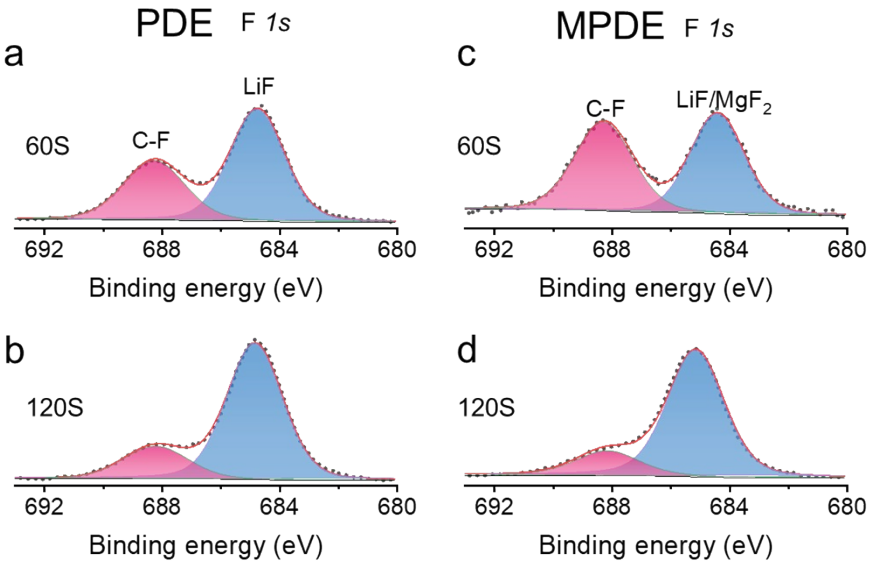

Fig. S20 The F *1s* XPS results for NCM811 cathodes cycling with PDE and MPDE at different etching times.

Fig. S21 Digital photograph of the PDOL electrolyte formed by $Mg(CH_3COO)_2$.

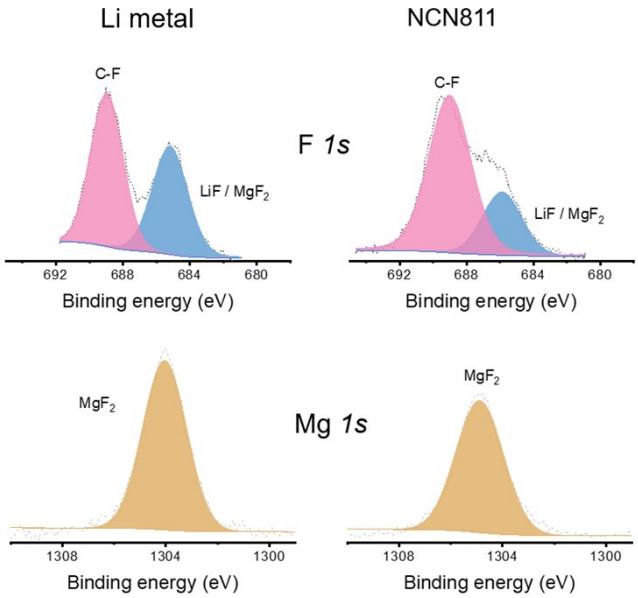

Fig. S22 XPS spectra of F *1s* (up) and Mg *1s* (down) for cycled Li metal (left) and NCN811 (right) with $Mg(CH_3COO)_2$-PDOL electrolyte.

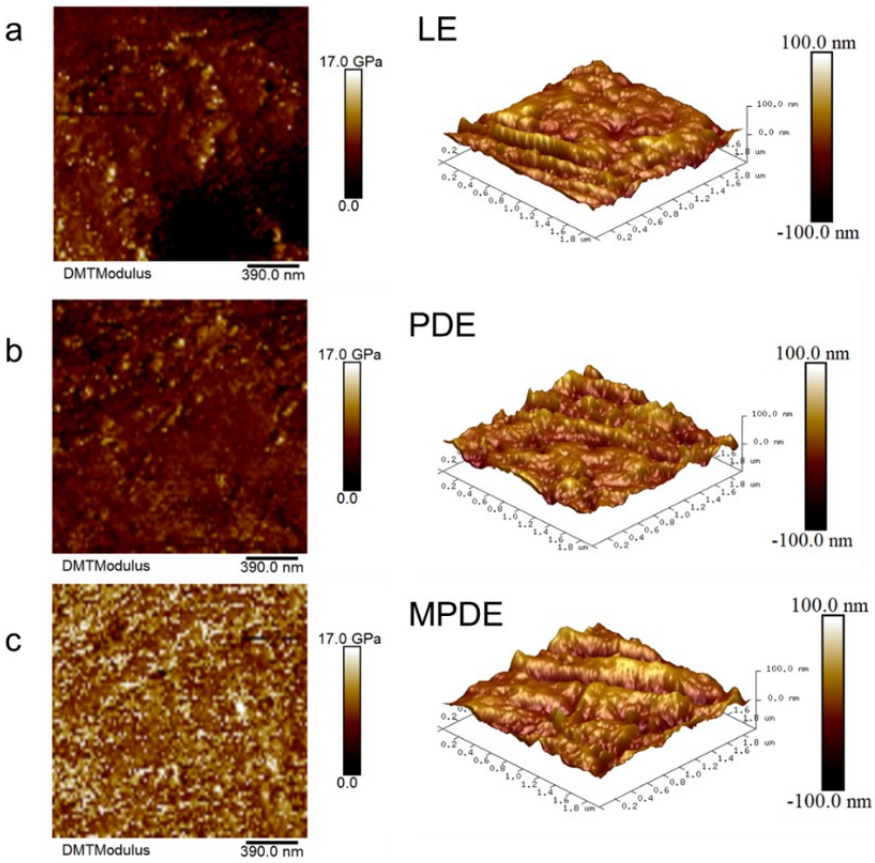

Fig. S23 Young's modulus and surface roughness of SEI induced by (a) LE, (b) PDE and (c) MPDE measured by atomic force microscopy (AFM).

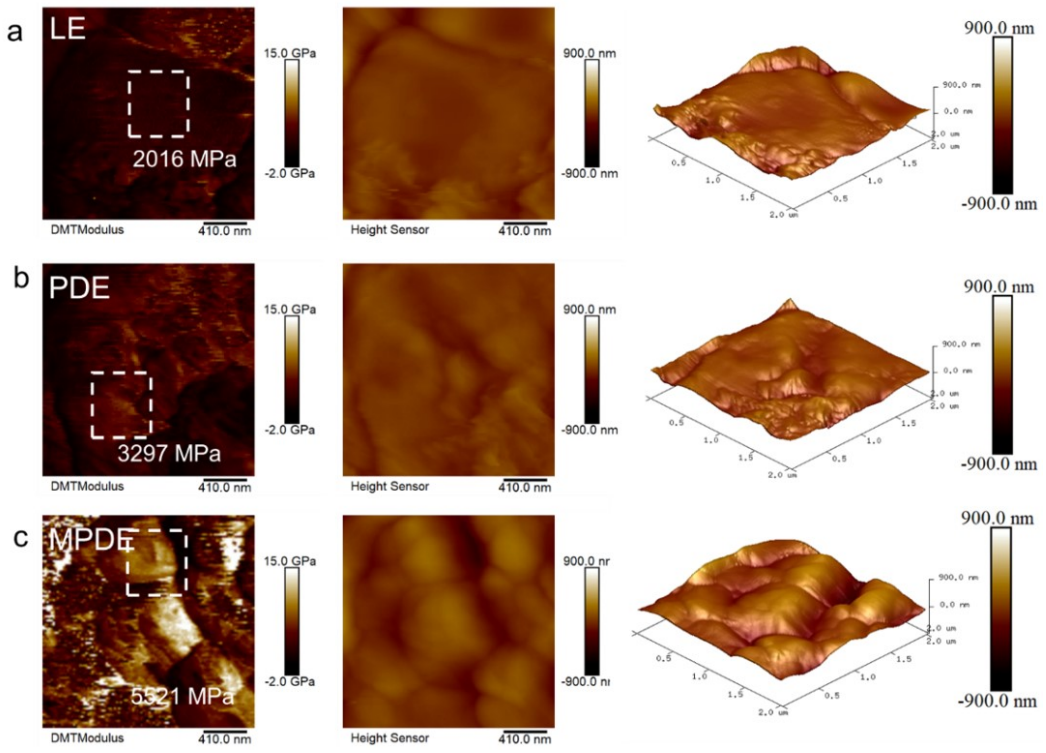

Fig. S24 Young's modulus and surface roughness of CEI induced by (a) LE, (b) PDE and (c) MPDE measured by atomic force microscopy (AFM).

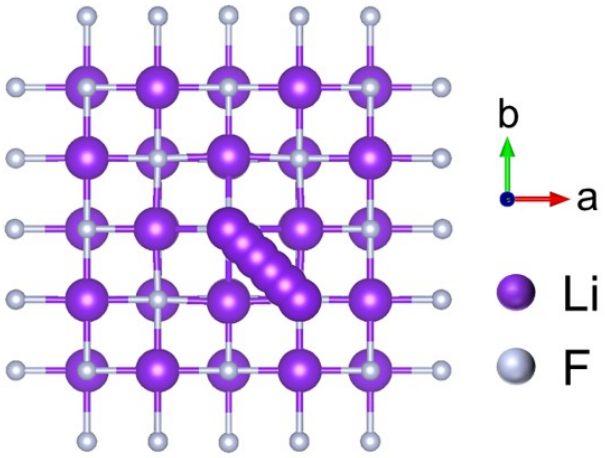

Fig. S25 Possible Li^+ diffusion paths of LiF.

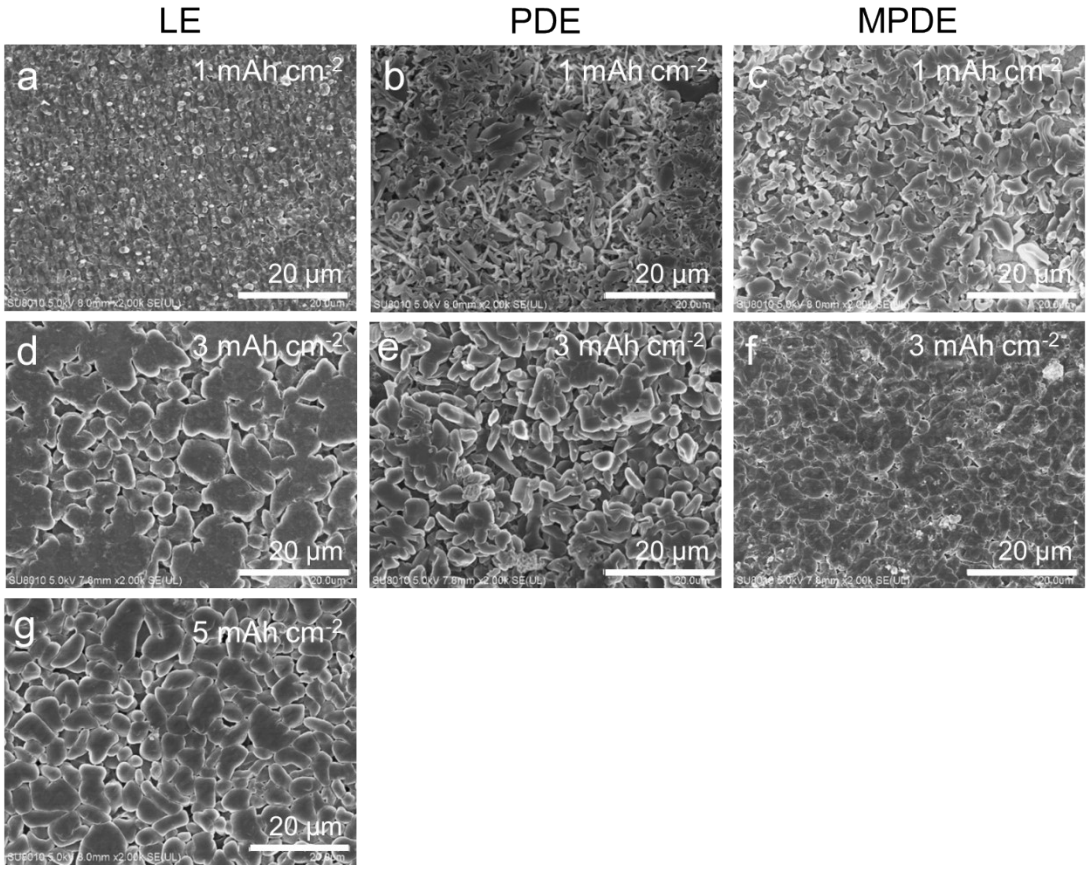

Fig. S26 SEM images of cycled Li anodes collected from symmetrical Li cells utilizing (a) LE, (b) PDE and (c) MPDE after plating 1 mAh cm^{-2}; (d) LE, (e) PDE and (f) MPDE after plating 3 mAh cm^{-2}; (g) LE after plating 5 mAh cm^{-2}.

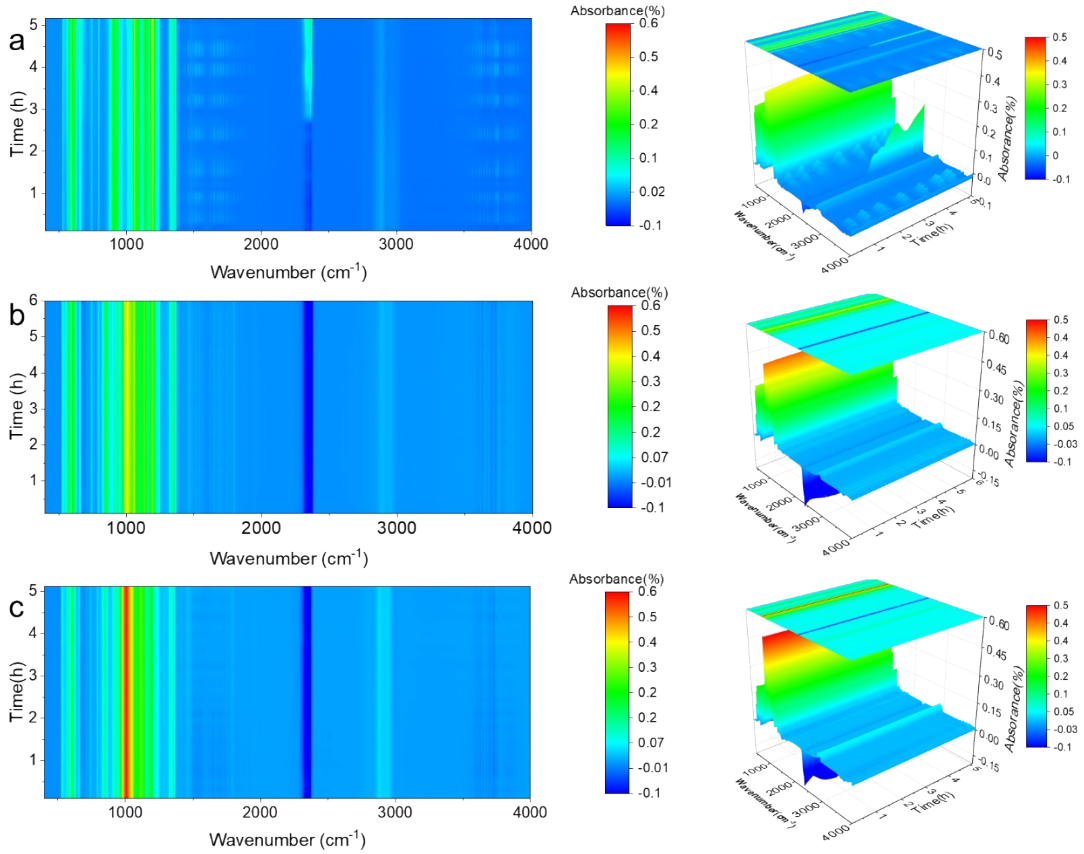

Fig. S27 In situ FTIR spectroscopy analysis of the (a) LE-NCM811, (b) PDE-NCM811 and (c) MPDE-NCM811 interface during charging and discharging.

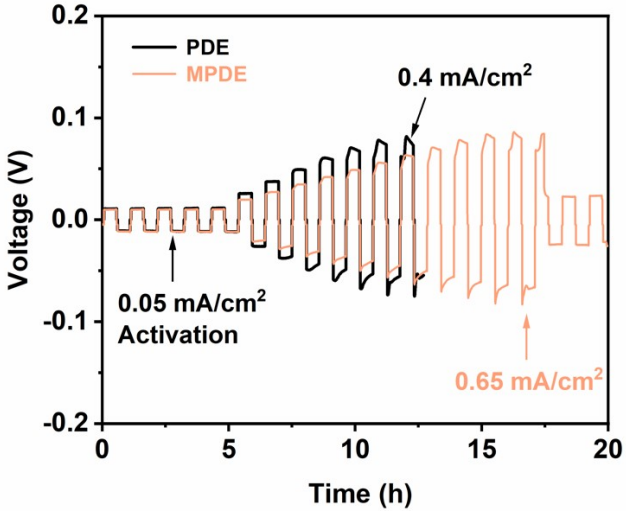

Fig. S28 Critical current density test of Li/Li symmetric cells using PDB and MPDE.

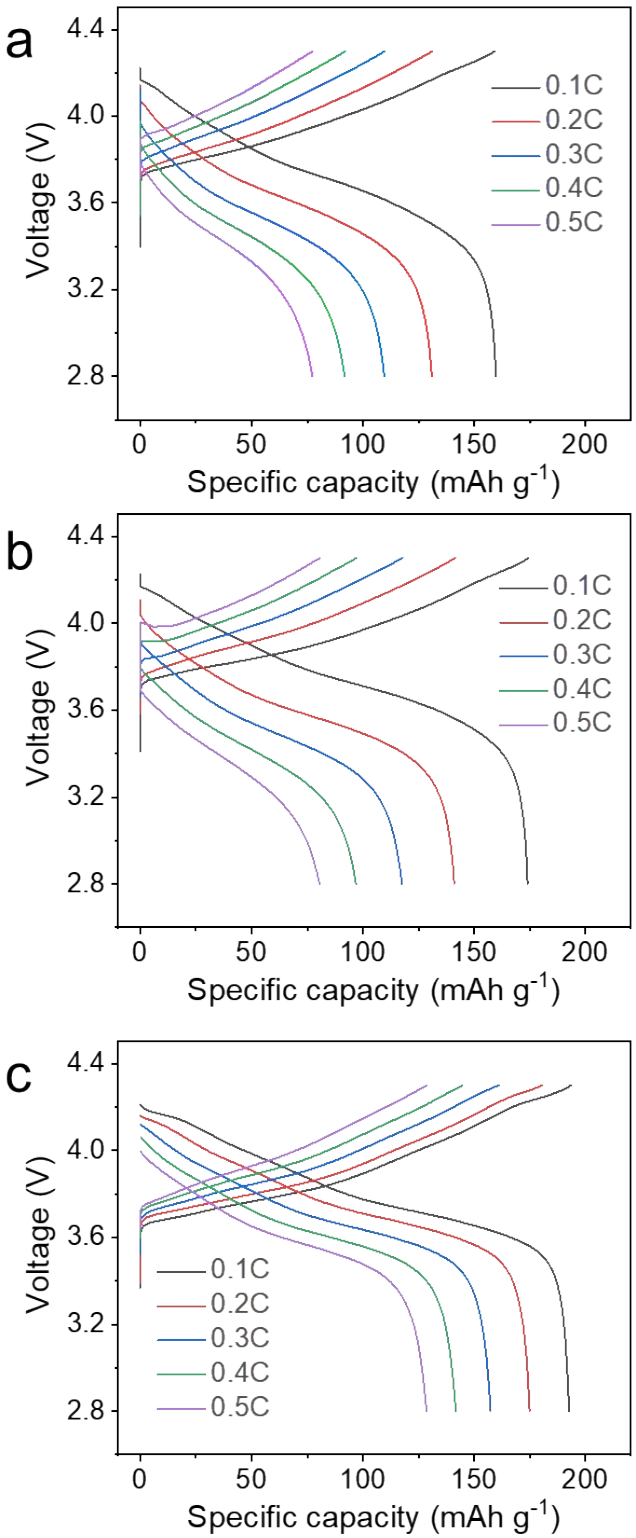

Fig. S29 Charge/discharge profiles for Li/NCM811 cells using (a) LE, (b) PDE, and (c) MPDE at 0.1, 0.2, 0.3, 0.4 and 0.5 C.

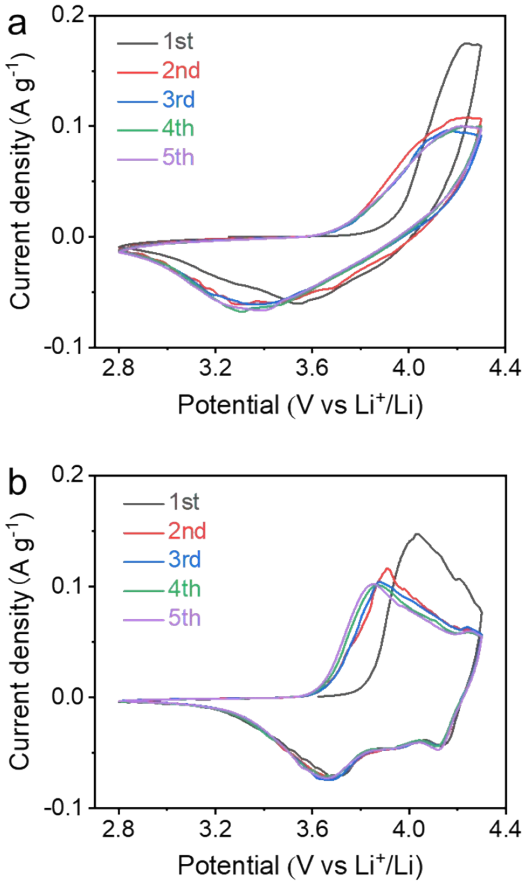

Fig. S30 The cyclic voltammetry (CV) curves of (a) NCM811/PDE/Li cell and (b) NCM811/MPDE/Li cell.

Table S1. The calculated LUMO and HOMO energies

Components	LUMO (eV)	HOMO (eV)
$TFSI^-$	4.30	–4.08
$DFOB^-$	2.76	–3.06
LiDFOB	–2.07	–7.81
LiTFSI	–1.41	–8.81
PDOL-$DFOB^-$	1.16	–4.47
PDOL-$TFSI^-$	2.94	–4.53
PDOL-LiDFOB	–1.45	–6.65
PDOL- LiTFSI	–1.84	–6.97
PDOL5	1.02	–7.04
PDOL10	1.00	–7.03

Table S2. Comparative data of Li-metal batteries cycling performance of our work with previously published studies

Electrolyte	Current density (mA cm^{-2})				
	0.1	0.2	0.25	0.4	0.5
PDOL-LATP[11]	500	--	--	--	--
TPDOL[12]	--	1800	--	--	--
PDOL-LLZTO[13]	--	600	--	--	--
PDOL-Al_2O_3[14]	--	1600	--	--	300
PDOL-LLTO[15]	900	--	--	--	--
SN-CPE[16]	1500	550	--	--	--
PDOL-YSZ[17]	1200	--	--	750	--
PDOL-PDA/PVDF-HFP[18]	--	--	800	--	250
This work (MPDE)	6000	2000	--	--	800

References

1. P. E. Blöchl, *Phys. Rev. B*, 1994, **50**, 17953.
2. G. Kresse and J. Hafner, *Phys. Rev. B*, 1993, **47**, 558-561.
3. G. Kresse and J. Hafner, *Phys. Rev. B*, 1994, **49**, 14251-14269.
4. K. G and F. J, *Comput. Mater. Sci.*, 1996, **6**, 15-50.
5. K. G and F. J., *Phys. Rev. B*, 1996, **54**, 11169-11186.
6. P. JP, B. K and E. M, *Phys. Rev. B* 1996, **77**, 3865-3868.
7. G. Henkelman and H. Jónsson, *J. Chem. Phys.*, 2000, **113**, 9901-9904.
8. S. Grimme, J. Antony, S. Ehrlich and H. Krieg, *J Chem Phys*, 2010, **132**, 154104.
9. P. Wei, Y.-Y. Zheng, Y. Xiong, S. Zhou, K. Al-Zaoari and A. Zaoui, *Applied Clay Science*, 2022, **228**, 106622.
10. A. V. A. F. G. G. Artioli, *American Mineralogist*, 2002, **87**, 10.
11. Z.-h. Huang, M.-x. Jing, P.-q. Wang, W.-w. Shao, Z.-p. Zhang, G. Zhang and X.-q. Shen, *Ceram. Int.*, 2023, **49**, 5510-5517.
12. S. J. Yang, H. Yuan, N. Yao, J. K. Hu, X. L. Wang, R. Wen, J. Liu and J. Q. Huang, *Adv. Mater.*, 2024, 2405086.
13. L.-H. Chen, Z.-Y. Huang, S.-L. Chen, R.-A. Tong, H.-L. Wang, G. Shao and C.-A. Wang, *Rare Met.*, 2022, **41**, 3694-3705.
14. J. Ma, Y. Wu, H. Jiang, X. Yao, F. Zhang, X. Hou, X. Feng and H. Xiang, *Energy Environ. Mater.*, 2023, **6**, e12370.
15. S. Zheng, Y. Chen, K. Chen, S. Yang, R. Bagherzadeh, Y.-E. Miao and T. Liu, *J Mater. Chem. A*, 2022, **10**, 19641-19648.
16. Z. Ren, J. Li, M. Cai, R. Yin, J. Liang, Q. Zhang, C. He, X. Jiang and X. Ren, *J Mater. Chem. A*, 2023, **11**, 1966-1977.
17. H. Yang, B. Zhang, M. Jing, X. Shen, L. Wang, H. Xu, X. Yan and X. He, *Adv. Energy Mater.*, 2022, **12**.
18. D. Chen, M. Zhu, P. Kang, T. Zhu, H. Yuan, J. Lan, X. Yang and G. Sui, *Adv. Sci.*, 2022, **9**, 2103663.